

MICRO-VIEW ASSESSMENT OF ELASTO-PLASTIC DEFORMATION CHARACTERISTICS OF GRAVELLY SOILS USING DISCRETE ELEMENT METHOD

Thi Kim Thoa Ho¹ and Meng-Chia Weng^{2*}

ABSTRACT

Owing to rapid city development on gravelly formations, it is essential to evaluate the mechanical behavior of gravelly soil and predict its deformational response during construction. This study adopted the discrete element method to simulate the large-scale triaxial test of gravelly soil to elucidate the deformational behaviors, including nonlinear elastic and significant plastic deformation of gravelly soil. The results revealed that the simulated failure envelopes and stress-strain curves agreed with the test results. Considering the influence of the micro properties on the elastoplastic deformation characteristics, a higher plasticity index of the matrix decreases the elastic shear modulus. The particle shear stiffness and aspect ratio were the main factors that affected the variations in the plastic flow angle. The porosity and particle effective modulus significantly affected the plastic trajectory as observed in the plastic strain trajectory analysis. It was found that the denser the specimen and the larger the particle effective modulus, the smaller the plastic strain trajectory.

Key words: gravelly soil, discrete element method, stress path, microscopic properties, elastoplastic deformation.

1. INTRODUCTION

Gravelly soil is a composite material with gravel and matrix contents. The content and external shape of the gravel (such as angular, subangular, subrounded, rounded, and well-rounded shapes) vary considerably from region to region (Mitchel and Soga 2005; Rücknagel *et al.* 2013). Many previous studies have investigated the complex characteristics of gravelly deposits compared to other individual soils because of the combination of gravel and matrix. The mechanical behavior of gravelly soil is dominated by gradation, void ratio, size effect, and water content (Holtz 1961; Marsal 1967; Mariachi 1969; Charles and Watts 1980; Matheson 1986; Indraratna *et al.* 1998; Chu *et al.* 2010).

Owing to rapid city development in central Taiwan, many construction projects located in gravelly formations have recently increased. This study investigates the behavior of natural gravelly deposits in central Taiwan, known as the Toukoshan Formation of the Pliocene Epoch. A large amount of gravel can be observed on top of the tableland. However, the texture of the gravel layer is relatively loose, and the matrix, including sand, silt, and clay, are filled between the gravels (Fig. 1). The gravelly deposits are classified as transitional rockfill material by Matheson (1986) because of a low fine content (such as silt and clay) and a high content of coarse-grained soil. The mechanical behavior of gravelly soil may affect the stability of deep excavation, foundation, and tunneling. Therefore, it is essential to evaluate the mechanical behavior of gravelly soils and establish an advanced model to predict their response during construction.



Fig. 1 The Toukoshan Formation—A typical of gravelly soils in Taiwan

For gravelly soils with a wide range of size distributions, experimental testing with large-scale triaxial tests faces many difficulties owing to the limitations of equipment and cost. Therefore, the discrete element method (DEM), which is widely applied in geotechnical engineering, is considered a solution for analyzing gravelly soil behavior. Macroscopic geomaterial behavior can be simulated from the interactions of microscopic components in the discrete element method (DEM): a model for rock (Potyondy and Cundall 2004); analyzing the interaction between granular material blades (Coetzee and Els 2009); behavior of gap graded soils Gong *et al.* 2019); triaxial test simulation for sand (Kozicki *et al.* 2014); crushable sand characteristics (Bono and McDowell 2014); deformation and

Manuscript received March 29, 2023; revised May 26, 2023; accepted July 6, 2023.

¹ Ph.D., Faculty of Civil Engineering, College of Engineering, Can Tho University, Cantho City 94000, Vietnam.

^{2*} Professor (corresponding author), Department of Civil Engineering, National Yang Ming Chiao Tung University, Hsinchu 30010, Taiwan (e-mail: mcweng@nycu.edu.tw).

degradation of fouled ballast (Ngo and Indraratna 2020); triaxial test simulation for glass beads (Hazzar *et al.* 2020); rock creep in tunnels (Gutiérrez *et al.* 2021); cyclic liquefaction behavior of cemented sand (Zhang *et al.* 2021), and concrete behavior (Nitka and Tejchman 2015). The particle content, particle size, packing, and particle shape (sphericity, aspect ratio, and particle roundness) (Minh and Cheng 2013; Gan *et al.* 2018; Tian *et al.* 2018; Cil *et al.* 2020; Gan and Yu 2020; Feng *et al.* 2021; Wu *et al.* 2021) and stress path, cyclic loading, and boundary conditions (Qian *et al.* 2016; Qu *et al.* 2019; Yang *et al.* 2019; Hossain *et al.* 2007; Dahal and Mishra 2020; Li *et al.* 2020) have been considered in recent studies. Ho and Weng (2021) used a 2D DEM to simulate the stress-strain relationship of gravelly soils through a triaxial test with a pure shear stress path. The simulation results were consistent with the experimental results, and the effect of the input parameters on the macroscopic properties of gravelly soil was also evaluated explicitly.

However, to reflect the actual specimen shape and its stress state of the triaxial test, this study extends the results of Ho and Weng (2021) and performs 3D DEM analysis to investigate the elastoplastic deformation of gravelly soil. First, a series of conventional triaxial tests on gravelly soils from Weng *et al.* (2013) were adopted to validate the DEM simulations. Then, the loading-reloading triaxial test simulations analyzed the elastoplastic deformation of the gravelly soil. Finally, the effects of the microscopic properties on the macroscopic elastoplastic deformation were explored.

2. NUMERICAL MODELING OF TRIAXIAL TEST ON GRAVELLY SOILS

2.1 Laboratory Tests

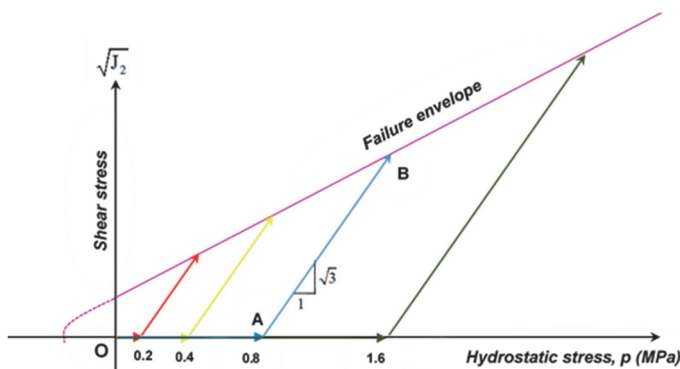
The conventional triaxial compression (CTC) test results from Weng *et al.* (2013) were adopted to analyze the elastoplastic deformation behavior of gravelly soils. In the specimen, the gravel component (particle size > 4.75 mm) has a specific gravity of 2.61 and a subrounded particle angularity. According to petrographic analysis, its primary lithology was quartzite and sandstone. For specimen preparation, gravelly soil was manually remolded from natural gravelly deposits collected from central Taiwan. These deposits have gravel particles of a wide range of sizes. The largest gravel particles are up to hundreds of millimeters. They do not meet the equipment limitations for large-scale triaxial tests;

therefore, the maximum gravel particle size in these remolded specimens was scaled down to 50.8 mm. Two typical gravelly soil samples were classified as follows based on the fine content: group A (plasticity index, PI = 0) and group B (PI = 22), which contained 8.7% and 11.3% fine content, respectively. According to soil classifications of the Unified Soil Classification System (USCS) and AASHTO, these samples have a high uniformity coefficient of approximately 85.8. Based on USCS, Group A is classified as GP-GM, and Group B is classified as GP-GC. In the AASHTO classification system, Group A is A-1-a, and Group B is A-2-6 (Chu *et al.* 2010; Weng *et al.* 2013). In Taiwan, the terms gravel and matrix were commonly used in gravelly soils, while the smaller particles have relatively low cementation and strength (Chang and Cheng 2014) in which the particles coarser than 4.75 mm are regarded as gravel, and the matrix represents the particles finer than 0.075 mm.

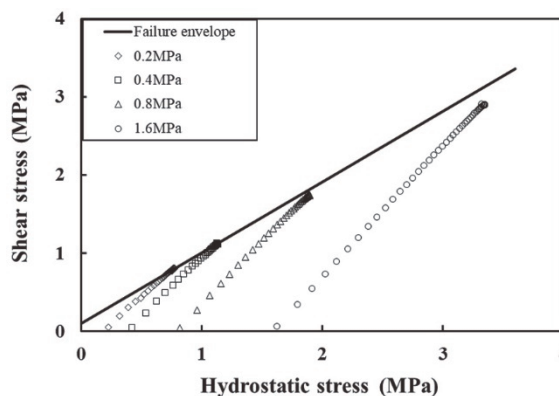
The recreated samples of groups A and B were compacted in five layers, conforming to the modified Proctor compaction test, until the large specimen size was 61.0 cm in height and 30.5 cm in diameter. The drained triaxial tests were executed as a series with various confining pressure rates after these samples were completely saturated when the pore pressure parameter B reached 0.95 (Chu *et al.* 2010; Weng *et al.* 2013). In the CTC test, the hydrostatic stress path was applied to the specimens as the OA path (Fig. 2); subsequently, the deviatoric stress path was applied (AB path). One test with three cycles of unloading and reloading (corresponding to 30%, 55%, and 80% of the ultimate strength) was conducted to elucidate the elastic deformation behavior.

2.2 Specimen Modeling

For the DEM simulation in this study, these large specimens of gravelly soils were simulated as cylinder samples using the Particle Flow Code software in 3D version 5.0 (PFC3D) (Itasca Consulting Group Inc 2016). For simplicity and time efficiency, the soil particles, which included gravel particles and the matrix, larger and smaller than 4.75 mm (Chang and Cheng 2014; Chang *et al.* 2015), respectively, were generated as spherical balls. The volume fractions of gravel were considered as the grain-size distribution curve, and the largest and smallest particles could be determined from this curve. Simultaneously, the lower size limit was scaled up to 4.74 mm (Fig. 3(a)). Finally, the representative sample contained 194,232 balls with 20% porosity, which was expressed for the large-scale specimen (Fig. 3(b)).

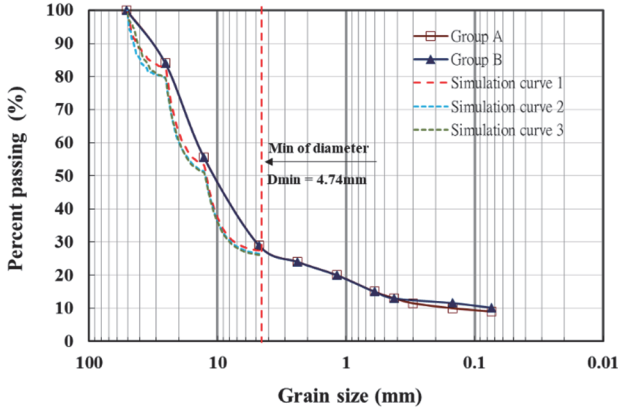


(a)

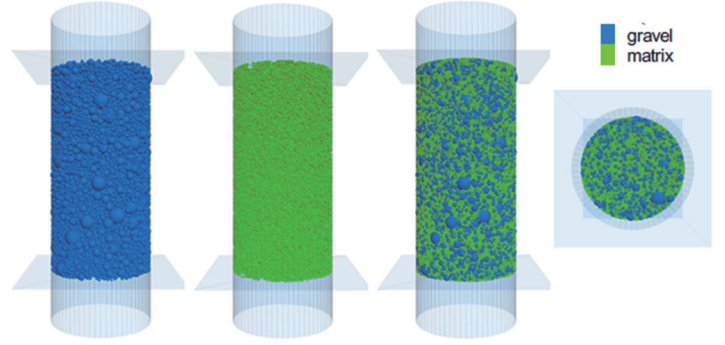


(b)

Fig. 2 (a) The CTC test in the schematic illustration chart; (b) The CTC paths in simulation



(a) Grain size distribution curves of gravelly soils in simulation



(b) The distribution of gravel and matrix particles in 3D large-scale triaxial test simulation

Fig. 3 Particle size distribution curves and calibration curves for PFC3D

A rigid wall boundary was assumed for large-scale triaxial simulation. The lateral cylinder wall simulated the membrane of a large-scale triaxial specimen. The top and bottom walls modeled the test loading plates subjected to equal and opposite constant velocities for a strain-controlled compression test. For the radial wall, during the isotropic consolidation stage, the velocities of the radial facets were adjusted to achieve the target confining stress using the servo-control mechanism, which was maintained as constant confining stress during the compression stage. Applying an axial load to the sample is controlled by moving the top and bottom loading plates of the model while maintaining a constant confining pressure. (Lan *et al.* 2021). External forces were exerted on the outer layer of the particles in the sample using the servo control mechanism on a rigid wall. A relatively uniform stress distribution within a specimen could be obtained iteratively (Qu *et al.* 2019).

2.3 Contact Model Between Particles

To reflect the mechanical properties of the fine content, a linear parallel bond model was adopted for the two types of specimens (Table 1). Three specified soil samples were created to evaluate the rationale of preparing samples for modeling: dense, loose, and medium loose packing. According to Liu *et al.* (2019), relative density in soil mechanics represents soil compactness. When DEM

Table 1 Microscopic parameters for gravelly soil triaxial test

Parameters	Unit	Group A (PI = 0)	Group B (PI = 22)
Number of particles		194,232	194,232
Max. radius of particles	mm	25.6	25.6
Min. radius of particles	mm	2.35	2.35
Density of particles, γ_d	kg/m ³	2150	2150
Ball-facet contacts (linear model)			
Effective modulus, E^*	MPa	350	350
Normal-shear stiffness ratio, k^*		1.0	1.0
Particle friction coefficient μ		0.3	0.3
Ball-ball contacts (linear parallel bond model)			
Effective modulus, E^*	MPa	400	200
Normal-shear stiffness ratio, k^*		1.0	1.0
Particle friction coefficient μ		0.5	0.5

Bond effective modulus, \bar{E}^*	MPa	0.4	0.35
Bond normal-shear stiffness, \bar{k}^*		1.0	1.0
Bond tensile strength, pb_ten	MPa	1.0	1.0
Bond cohesion, pb_coh	MPa	1.0	1.0
Bond gap	m	5×10^{-4}	5×10^{-4}

was used to simulate particle packing, a relationship was observed between the friction coefficient and relative density. Consequently, granular materials with varying compactness could be produced by varying the friction coefficient of the particles.

The distinct difference between these specimens was the interparticle friction coefficients (μ) during ball generation because the inter-friction coefficient significantly impacts packing results. A higher friction coefficient causes faster kinetic energy loss, resulting in looser particle packing. The values $\mu = 0.01$, $\mu = 0.5$, and $\mu = 0.8$ were assigned to dense, medium loose, and loose packings, respectively. The initial porosity applied to these specimens was the same, $n = 20\%$. After applying the friction coefficient, the porosities of the dense, medium, and loose packings were $n = 19\%$, 21% , and 22% , respectively.

The results show that the behavior of the medium loose sample ($\mu = 0.5$) was in good agreement with the test results (Weng *et al.* 2013). The soil strength was extremely high; however, the stress-strain curve exhibited softening behavior in the case of the dense sample. Because the difference between the sizes of particles was significant, the proximity distance (or bond gap) described the minimal space at which contacts were used in positive values. Different cases of the bond gap are compared in Fig. 4. These results may be attributed to the low cemented characteristics of the simulated gravelly soil.

Drucker-Prager plasticity model is developed by combining yield and plastic potential functions into a working elasto-plastic model for elasto-plastic materials (Fattah *et al.* 2012). For the convenience of material modeling, the stress tensor was decomposed into a hydrostatic stress tensor and a deviatoric stress tensor. To consider the failure criterion, the Drucker-Prager criterion was adopted, which can be expressed as:

$$f(I_1, J_2) = \alpha I_1 + \sqrt{J_2} - k = 0 \quad (1)$$

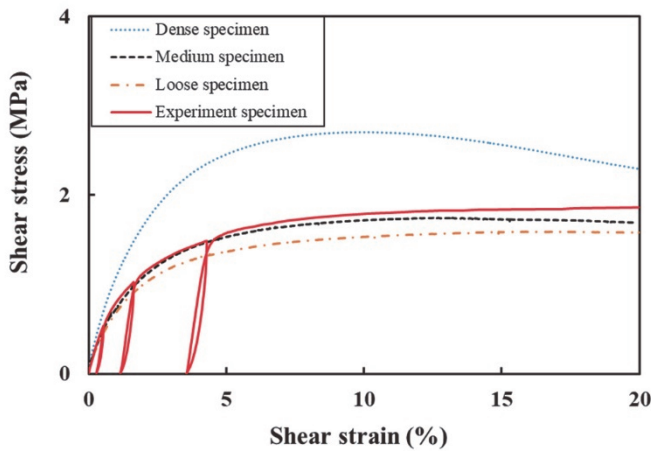
where $\sqrt{J_2}$ is the shear stress, I_1 is the first invariant, $I_1 = \sigma_1 + \sigma_2 + \sigma_3$ ($\sigma_1, \sigma_2, \sigma_3$: principal stresses), α is the slope of

the failure envelope, and k is the cohesive intercept of the failure envelope.

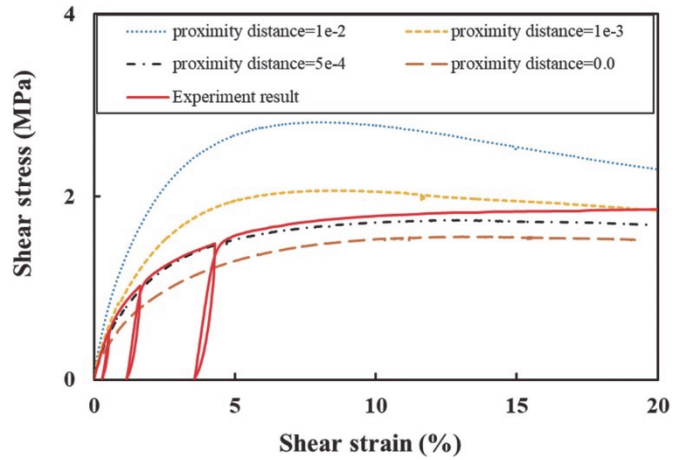
In Eq. (1), the shear stress ($\sqrt{J_2}$) can be determined using the deviator tensor, and in the triaxial test, the term $\sqrt{J_2}$ can be

described by Eq. (2):

$$\sqrt{J_2} = \frac{1}{\sqrt{6}} [(\sigma_1 - \sigma_3)^2 + (\sigma_2 - \sigma_3)^2 + (\sigma_3 - \sigma_1)^2]^{1/2} \quad (2)$$



(a) Packing types



(b) Proximity distance

Fig. 4 Stress-strain behavior with different boundary conditions

Accordingly, shear strain ($2\sqrt{J_2}$) and volumetric strain (ϵ_v) can be determined using the following equations:

$$\gamma = 2\sqrt{J_2} = \frac{2}{\sqrt{6}} [(\epsilon_1 - \epsilon_3)^2 + (\epsilon_2 - \epsilon_3)^2 + (\epsilon_3 - \epsilon_1)^2]^{1/2} \quad (3)$$

$$\epsilon_v = \epsilon_{kk} = \epsilon_1 + \epsilon_2 + \epsilon_3 \quad (4)$$

3. VALIDATION OF THE EXPERIMENTAL RESULTS

3.1 Failure Envelope

Figure 5 shows the performance of the failure envelopes of the two gravelly soil groups. The simulated failure envelopes agree well with the experimental curves. The consistency between the simulation and experiment is evident for cases with smaller confining pressure levels (such as 0.2, 0.4, and 0.8 MPa). In the other cases ($p = 1.3$ and 1.6 MPa), the failure envelopes of the simulation slightly underestimate the experimental results.

Furthermore, from Fig. 5 it can be observed that the slope α of Group A ($\alpha = 0.316$) is higher than that for Group B ($\alpha = 0.302$), whereas the intercept k of Group A ($k = 0.01$) is significantly smaller than that of Group B ($k = 0.1$). The friction angle (ϕ) and cohesion intercept (c) of the Mohr-Coulomb failure criterion were converted from the Drucker-Prager failure criterion, and are summarized in Table. 2. From the Table. 2, the cohesion of Group A is trivial (approximately 9 kPa), Whereas that of Group B is significant (88 kPa). These results also prove that Group A is nonplastic gravelly soil whereas Group B is plastic gravelly soil.

3.2 Deformation Induced by Deviatoric Stress

Figure 6 depicts the relationship between the deviatoric stresses ($\sigma_1 - \sigma_3$) in the CTC test under various confining pressures. As shown in Fig. 6, when the applied confinement pressure increases, the initial stiffness also increases for all soil groups. The strain exhibits significant ductile behavior when the stress reaches the failure state. The correlation between the simulation and experimental results was reasonable for higher confining pressures, whereas for lower pressures ($p = 0.2$ MPa), the results differed slightly.

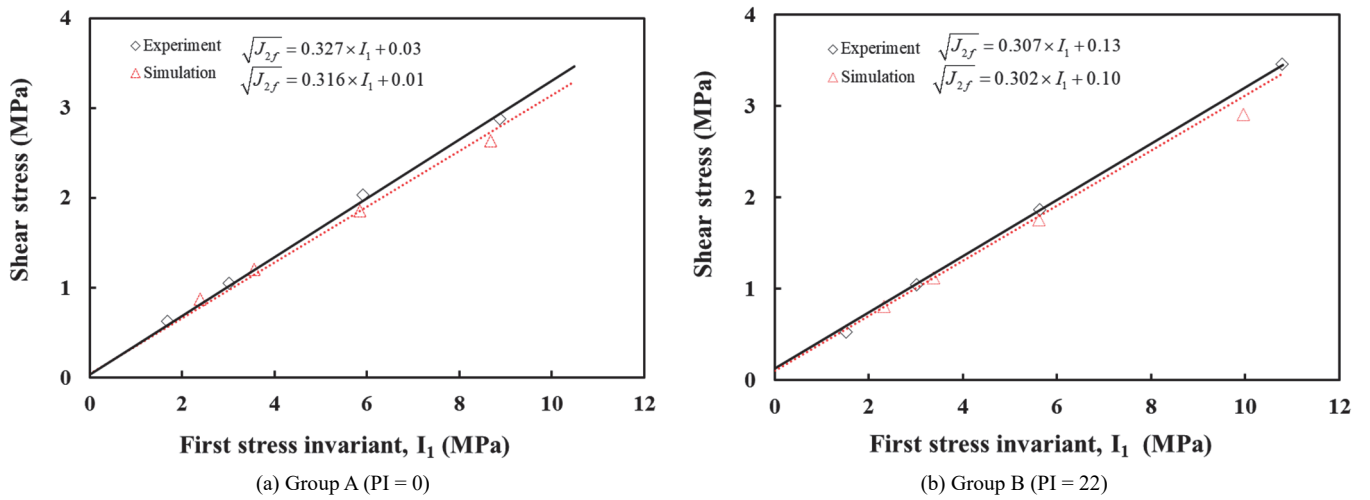


Fig. 5 Failure envelopes of simulated gravelly soils obtained by CTC test simulation

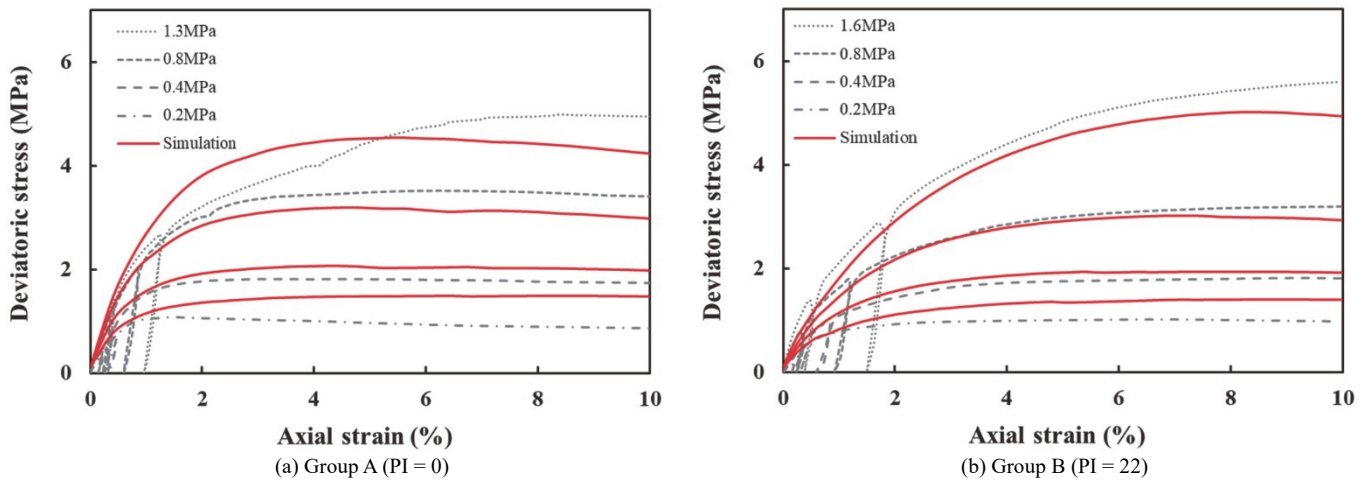


Fig. 6 Stress-strain curves of the CTC test corresponding to different confining pressure rates

The volumetric strain behavior of the two soil groups is shown in Fig. 7. When the compression stage occurred in Group A (Fig. 7(a)), the volumetric strains were initially contractive and gradually dilated as the shear stress increased. As the hydrostatic stresses increased, a greater dilation of the specimens occurred at the failure states. The volumetric deformations of Group B were similar to those of Group A. However, for the high confining

pressure rate ($p = 1.6$ MPa), the volumetric strain was almost only compressive when the stress reached the failure state (Fig. 7(b)).

A comparison of the strain magnitudes of the two soil samples is presented in Fig. 8. As shown in Fig. 8(a), with the same confining pressure ($p = 0.8$ MPa), the failure stress of group A (3.2 MPa) was marginally higher than group B (3.04 MPa). Moreover, this graph also reveals that group B is more ductile than group A;

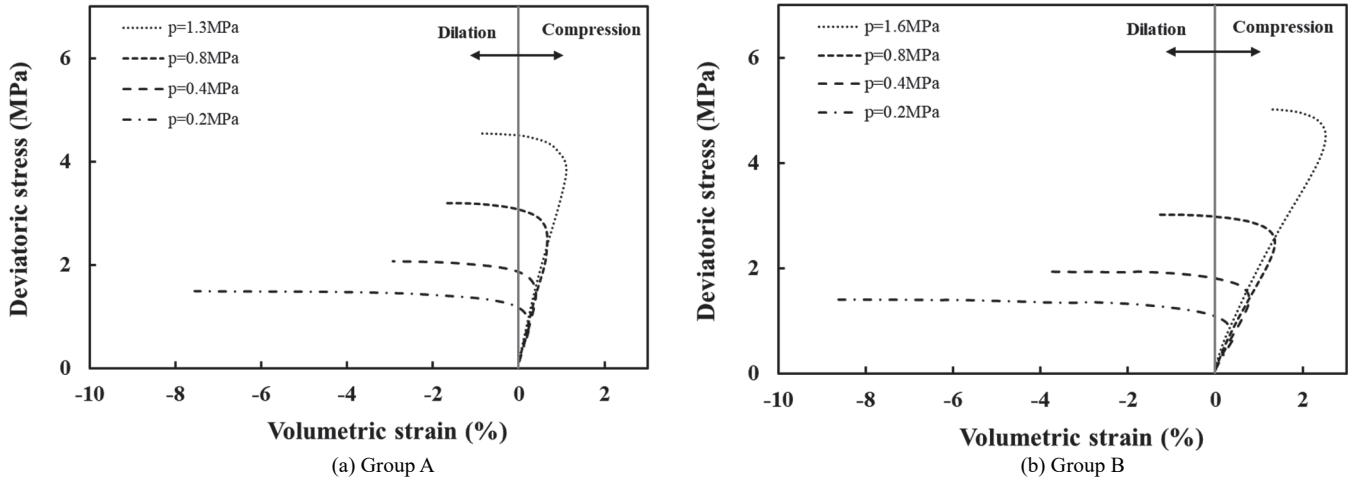


Fig. 7 Volumetric strain magnitudes in simulation with different confining pressure rates

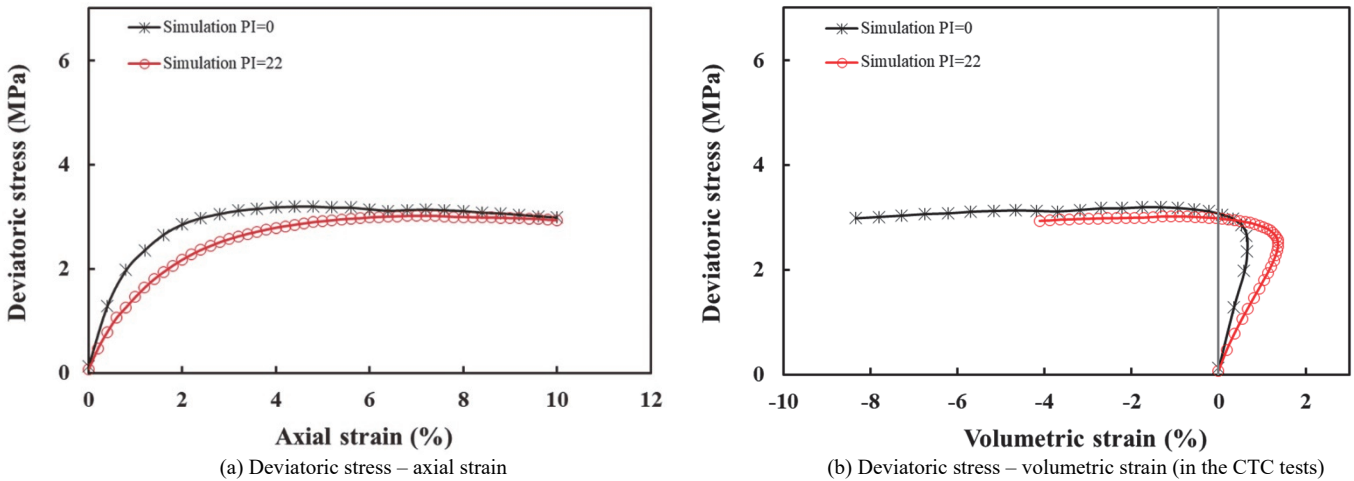


Fig. 8 Strain magnitudes in the comparison of DEM simulation of gravelly soils (for $p = 0.8$ MPa)

it is proved that when approaching the failure stress, the strain of group B ($\epsilon = 7.3\%$) was more extensive than that of group A ($\epsilon = 4.8\%$). Furthermore, the volumetric strain analysis (Fig. 8(b)) shows that the specimen in group B tends to be more compressive before it dilates than in group A. On the contrary, the sample in group A was enlarged by close to 10%, while the dilation of group B was 4%.

Figure 9 shows the actual and simulated failure patterns of the Group A and B specimens. The actual specimens exhibit bulge deformation in the central part of the specimens and no significant fractures are found (Figs. 9(a) and 9(b)). The simulated deformations of the two soil samples are shown in Figs. 9(c) and 9(d). The samples exhibited the same vertical compressive displacements. In contrast, the lateral displacement of sample group B was much smaller than that of sample group A. Then, the volumetric strain determined by Eq. (4) of sample group A was larger than that of sample group B. This made the sample compress vertically and bulge laterally, which agreed with the actual failure specimens.

3.3 Elastoplastic Deformation Characteristics

To analyze the deformations of the gravelly soils, each simulated CTC test included two cycles of loading and reloading

at 30% and 55% of the ultimate strength.

3.3.1 Elastic Shear Modulus

Based on the observed deformation behavior of gravelly soils in DEM simulations, this section explores the elastoplastic characteristics by dividing the total strain into two components: elastic and plastic strain tensors (Fig. 10).

$$\epsilon_{ij} = \epsilon_{ij}^e + \epsilon_{ij}^p \tag{5}$$

where ϵ_{ij} , ϵ_{ij}^e , and ϵ_{ij}^p are the total, elastic, and plastic strain tensors, respectively.

Regression-based loading-reloading curves at different stress stages can be used to determine the relationship between shear stress and elastic strain. Next, the plastic strain component was acquired by subtracting the elastic strain from the total strain. As shown in Fig. 10(a), the elastic component is always linear, whereas significant plastic shear strain occurs when the shear stress reaches the failure state. For the volumetric strain, the plastic strain had a tendency similar to that of the total strain: the strain was initially compressive, followed by significant dilation since the failure state occurred (Fig. 10(b)).

The variations in the elastic shear moduli (G) of the two

groups under various confining pressures are shown in Fig. 11. To obtain the elastic shear modulus for both soil groups, a function related to shear strain and the elastic shear strain was constructed as follows:

$$G = \frac{\sqrt{J_2}}{2\sqrt{J_2^e}} \tag{6}$$

where $\sqrt{J_2}$ is the shear stress and $\sqrt{J_2^e}$ is the second deviatoric strain invariant of elastic deformation.

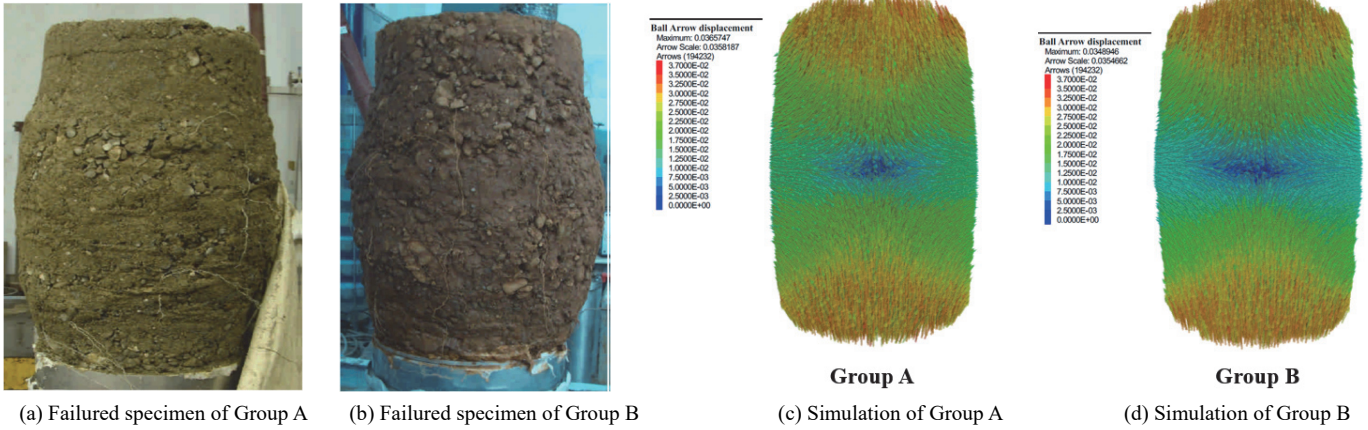


Fig. 9 Actual and simulated failure patterns of the Group A and B specimens

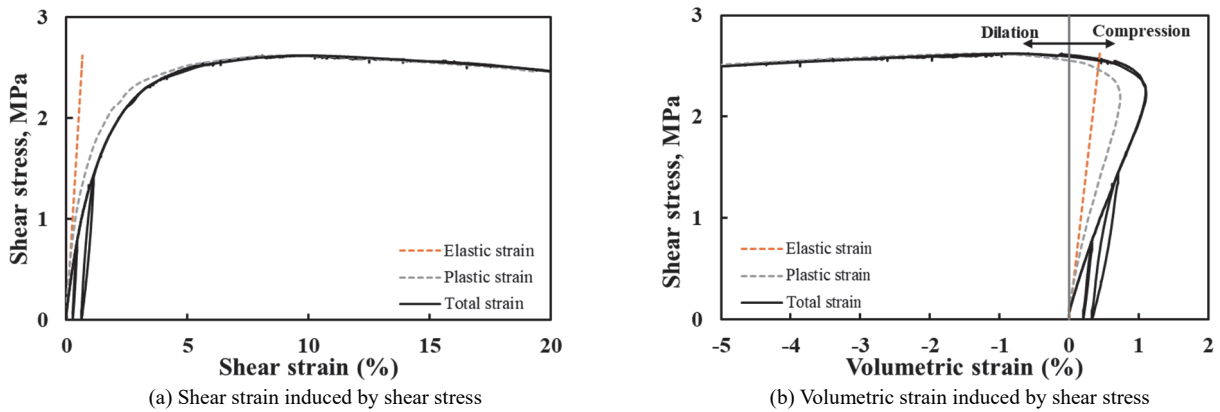


Fig. 10 Elastoplastic deformation analysis ($p = 1.3$ MPa)

Because the elastic deformation of group A was smaller than that of group B, whereas the shear stresses are not significantly different, the elastic shear modulus G of group A was higher than that of group B. The inset of Fig. 11 shows that the simulated elastic shear modulus ranged from 227 to 394 MPa for group A and 129 to 213 MPa for group B. The relationship between the elastic shear modulus (G) and confining pressure (p) can be expressed as a square root function of p . The simulation results were generally consistent with the experimental data, except for some discrepancies in group B.

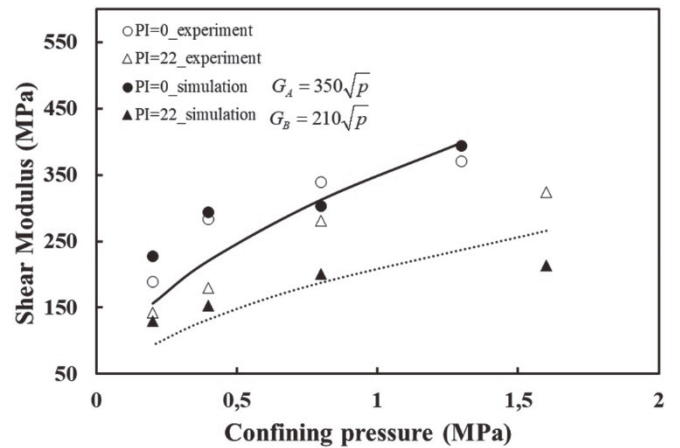


Fig. 11 Elastic shear modulus in simulations of gravelly soils with different confining pressure

3.3.2 Plastic Flow

As discussed in the previous sections, the plastic deformation of the gravelly soil also appeared before the specimen failed. To investigate the behavior of gravelly soils, strain increments were used to express the stress-strain relationship. After decomposing the strain increment into elastic and plastic parts, the direction and magnitude of the strain increment vector for the plastic part were calculated. Additionally, the flow rule, which includes the plastic potential function, was determined. If the plastic potential surface is the same type as the yield surface, it implies that it is an associated flow rule; otherwise, it is a non-associated flow rule.

First, the plastic shear strain (ϵ_s^p) and plastic volumetric strain (ϵ_v^p) were separated from the total strain ($\epsilon_s^{\text{total}}$ and $\epsilon_v^{\text{total}}$). The plastic shear strain increment and plastic volumetric strain increment were presented as $\delta\epsilon_s^p$ and $\delta\epsilon_v^p$, respectively. The direction and magnitude of the strain increment vectors were defined by the plastic flow angle (β) and plastic strain trajectory (ξ) (Eqs. (7) and (8)).

$$\tan\beta = \frac{\delta\epsilon_s^p}{\delta\epsilon_v^p} \quad (7)$$

$$\xi = \sqrt{\delta\epsilon_{ij}^p \delta\epsilon_{ij}^p} \quad (8)$$

where: $\delta\epsilon_{ij}^p$ is tensor of plastic strain increment.

The plastic flows of groups A and B are shown in Fig. 12. In both cases, plastic compression occurred early in the shearing process, followed by a counterclockwise transfer with high shear stresses. As the shear stress approached the failure envelope, the flow vector was perpendicular to the hydrostatic stress (p) axis and parallel to the shear stress ($\sqrt{J_2}$) axis. The final plastic flow direction was non-perpendicular to the failure envelope, implying that the plastic deformation of gravelly soils obeys a non-associated flow rule (Weng *et al.* 2013).

The plastic flow angle (β) and plastic strain trajectory (ξ) were further examined to clarify the plastic flow rule of the gravelly soils in both groups. As illustrated in Fig. 13, the angle of plastic flow (β) in the relationship with the shear stress ratio (η_f) was nonlinear and β gradually increased with η_f . The shear stress ratio (η_f) is defined as the ratio of shear stress to failure stress ($\eta_f = \sqrt{J_2} / \sqrt{J_{2,f}}$). The value of β was determined by the characteristic of the plastic volumetric strain increment ($\delta\epsilon_v^p$), $\delta\epsilon_v^p$ is considered compression when β ranges from 0 to 90°; otherwise, $\delta\epsilon_v^p$ is dilative. As shown in Fig. 13(a), the volumetric strain generally dilates when η_f is approximately 0.7 and the angle β is 90°. The same tendency can be observed in Fig. 13(b); when η_f is approximately 0.8, and the angle β is 90°, the volumetric strain becomes dilative. The figure also shows that the angle of plastic flow (β) is an independent variable of the confining pressure (p).

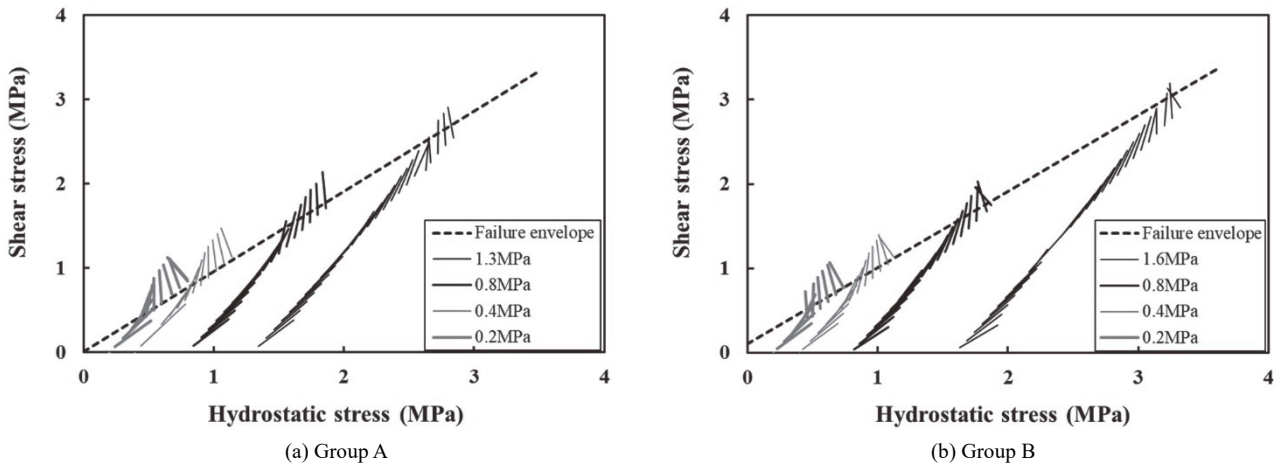


Fig. 12 Plastic flows during the CTC tests under various confining pressure rates

The variations in the plastic strain trajectory (ξ) of groups A and B, followed by the shear stress ratio (η_f) under various confining pressures, are shown in Fig. 14. Similar to the angle β , the confining pressures irregularly affect the plastic strain trajectories. Therefore, we can consider that the confining pressure has a negligible impact on the variations in the plastic strain trajectory ξ . According to the figure, the presence of plastic strains occurs early after the shearing begins; the strains appear to increase gradually until the shear stress approaches the failure state ($\eta_f = 0.8 - 1.0$), at which point the plastic strains increase rapidly. According to the above analysis results, the plastic flow angle and the plastic strain trajectory of soils in group A and group B have quite similar tendencies (Figs. 13 and 14).

4. MICRO-VIEW ANALYSIS ON ELASTO-PLASTIC DEFORMATION

To clarify the effects of the microscopic properties on the deformation of gravelly soils, a series of parametric studies are further conducted. These microscopic properties include porosity of the sample, the effective modulus of the particle, friction coefficient, and bond effective modulus. In addition, this study also considers the effect of gravel aspect ratio on elasto-plastic deformation of gravelly soils. Due to the similarity in elasto-plastic deformation of the two simulated soil samples, this section only discusses the influence of micro parameters on soil group B.

4.1 Effect of Porosity

A series of simulations in the case of $p = 0.8$ MPa were performed for varying porosity of the samples. The input parameters in Table 2 were adopted in these simulations, and the porosity values were set as 10%, 15%, 20%, 25%, and 30%.

Table 2 Macro properties of gravelly soils obtained from simulations

Parameters	Experiment	Simulation
Group A (PI = 0)		
Friction angle (Degree)	41.5	40.2
Cohesive interception (MPa)	0.027	0.009
Group B (PI = 22)		
Friction angle (Degree)	39.1	38.4
Cohesive interception (MPa)	0.114	0.088

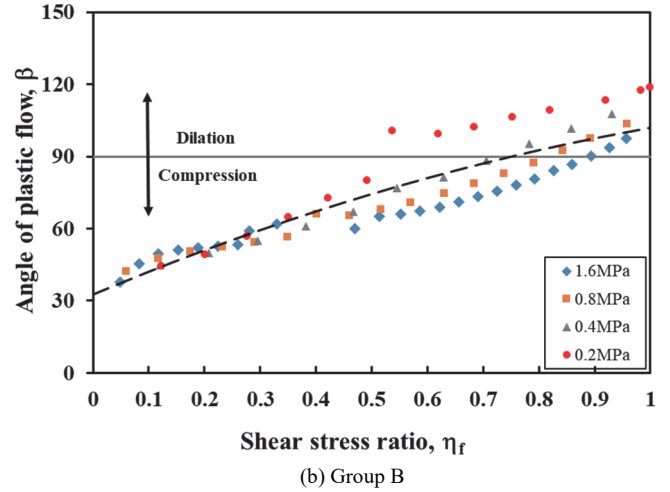
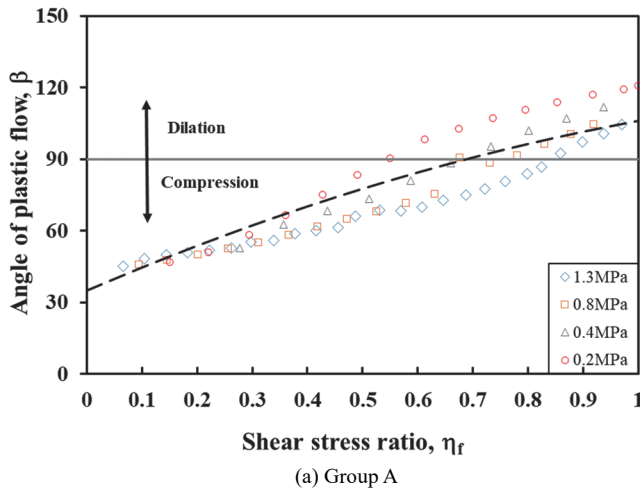


Fig. 13 Plastic flow angles of the CTC tests simulation under various confining pressure rates

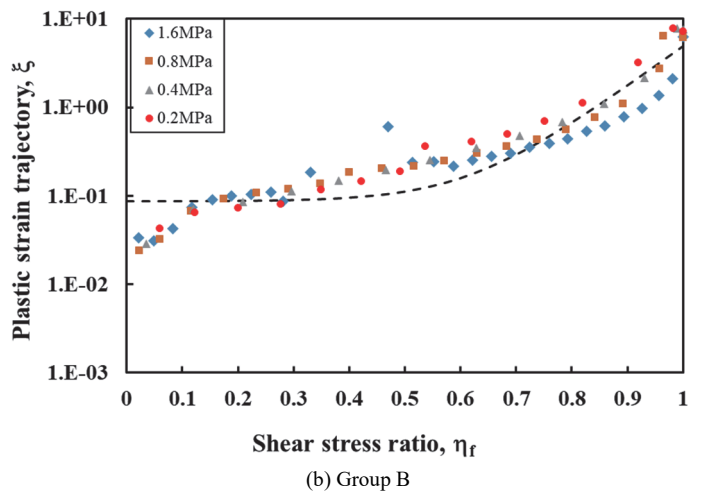
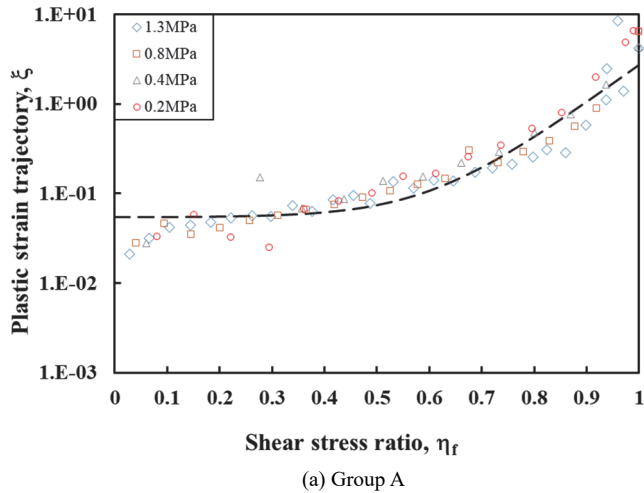


Fig. 14 Plastic strain trajectory in the CTC test simulation with different confining pressures

The relationship between the plastic flow angle (β) and shear stress ratio (η_f) is illustrated in Fig. 15(a). The relationship between β and η_f appears to be nearly identical, corresponding to varied porosities. This proves that the porosity is insignificant in the β and η_f relationships. The plastic flow angle β is less than 90° at low-stress ratios and gradually increased with the shear stress ratio η_f . When η_f reaches approximately 0.8 and $\beta = 90^\circ$, the volumetric deformation becomes dilative. In the failure state ($\eta_f = 1.0$), β exceeds 110° . However, the porosity has a significant impact on the plastic strain trajectory (ξ) (Fig. 15(b)). The dissimilarity in the plastic strain trajectory ξ under different values

of porosity increases with an increase in porosity. As shown in the figure, with low-stress ratios ($\eta_f < 0.7$), ξ increases very slowly; when the value of η_f is greater than 0.7, ξ increases gradually until it approaches the failure stress.

4.2 Effect of Effective Modulus of the Particle

The effect of the particle effective modulus (E^*) on the plastic deformation of gravelly soils was investigated. Similar to the porosity mentioned below, there is no evidence of any connection between E^* and the plastic flow angle β versus the stress ratio η_f

(Fig. 16(a)). With the same stress ratio η_f , the plastic flow angles for different cases of the particle effective modulus have negligible differences. However, when considering the effect of E^* on the plastic flow angle, the angle of plastic flow can reach 120° upon reaching the failure stress.

Figure 16(b) shows a typical mode of plastic flow trajectory ξ versus stress ratio η_f corresponding to different particle effective modulus parameters. The results highlight the role of E^* for ξ in the DEM simulation when considering the same value of η_f ; the

smaller the particle effective modulus, the larger the plastic strain trajectory.

4.3 Effect of Friction Coefficient

The friction coefficient (μ) is critical in the DEM analysis. A range of friction coefficients ($\mu = 0.2, 0.3, 0.5, 0.6,$ and 0.8) was applied in the simulation ($p = 0.8$ MPa) to investigate the role of μ on the plastic behavior of gravelly soils (Fig. 17).

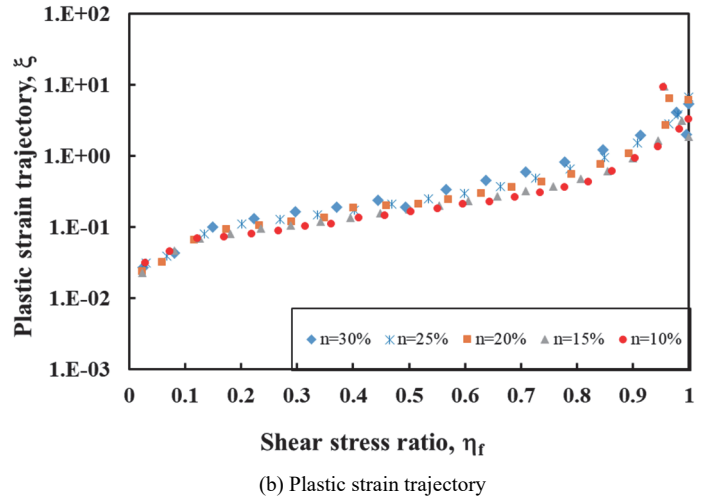
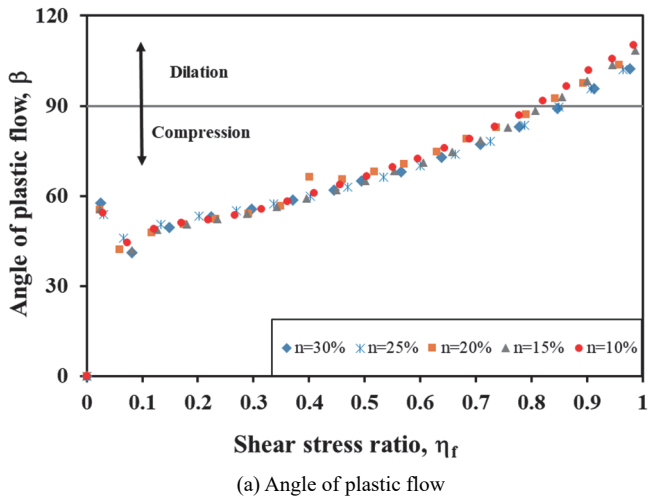


Fig. 15 Effect of sample porosity on plastic strain in DEM simulation

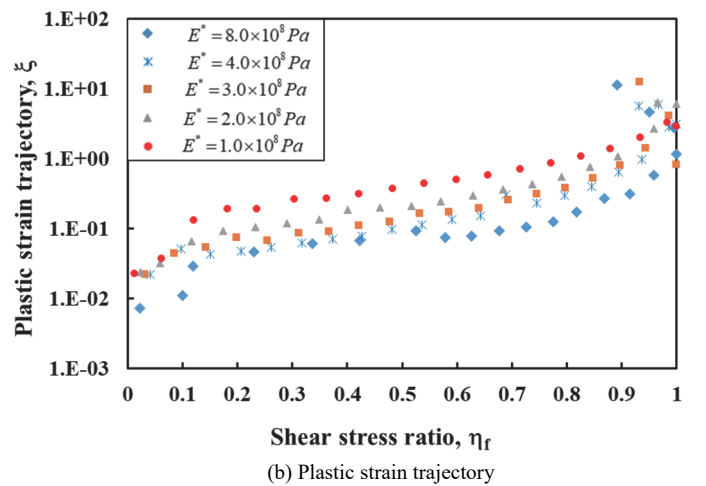
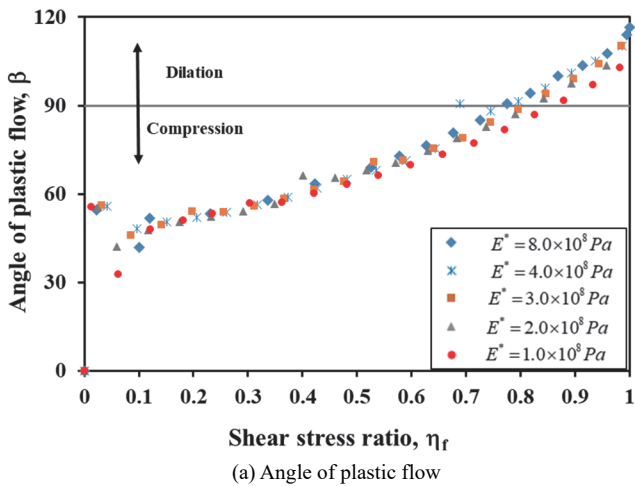


Fig. 16 Effect of particle stiffnesses (Effective modulus) on plastic strain behavior

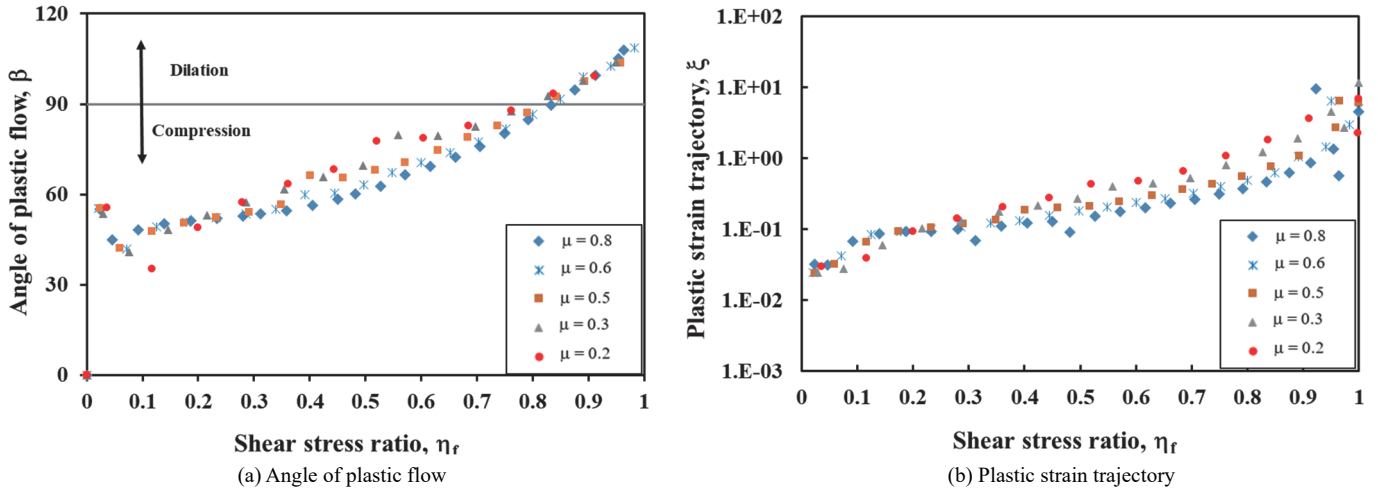


Fig. 17 Effect of friction coefficient on plastic strain behavior

For plastic flow angles (β) concerning the shear stress ratio (η_f), with the low-stress ratio ($\eta_f < 0.3$) as well as the high-stress ratio ($\eta_f > 0.8$), the plastic flow angle is almost the same regardless of the increase or decrease in the value of μ . When $0.3 < \eta_f < 0.8$, the plastic flow angle is larger for a smaller friction coefficient. When the stress reaches the failure envelope, β reaches a value close to 110° (Fig. 17(a)). Similarly, the impact of the friction coefficient on the plastic strain trajectory (ξ) is indicated only when $\eta_f > 0.3$. The increasing friction coefficient may decrease the plastic strain trajectory; however, this decrease is insignificant, as can be observed in Fig. 17(b).

4.4 Effect of Bond Modulus

The bond effective modulus (\bar{E}^*) values ranging from 0.15 to 0.8 MPa were used to evaluate this DEM simulation sensitivity. However, the bond effective modulus slightly affected the plastic flow angle when the shear stress ratio $\eta_f > 0.5$. Bond effective modulus could enhance the plastic flow angle with the same η_f ; $\bar{E}^* = 0.8$ MPa provided the largest plastic flow angle, whereas $\bar{E}^* = 0.15$ MPa provided the smallest plastic flow angle (Fig. 18(a)).

Figure 18(b) presents the characteristics of the plastic strain

trajectory in many different cases of the bond effective modulus. Unlike the other parameters analyzed, the plastic strain trajectory was not affected by the bond effective modulus. With cases $\bar{E}^* = 0.15, 0.35, 0.5, 0.65,$ and 0.8 MPa, the plastic strain trajectory values at the same stress ratio almost coincided.

4.5 Effect of Gravel Aspect Ratio

Many previous studies have used the ellipsoid model (Gong and Liu 2017), breakable particle model (Bian *et al.* 2016; Nie *et al.* 2023), and real shape model (Liu *et al.* 2021) to study the influence of the grain shape on the mechanical properties of granular materials because these particles reflect the realistic behavior of the materials. Ellipsoids offer a useful model for examining how particle form affects the mechanical behavior of granular materials (Gong and Liu 2017). The aspect ratio, which is defined as the ratio of the major axis to the minor axis of the particle, is an important shape factor for expressing the actual shape of granular materials. Yang *et al.* 2019 illustrated an ellipsoid in a laser beam to determine the change in particle orientation. The aspect ratio (AR) function is described as $AR = L/S$; where L and S are the longest and shortest particle lengths, respectively.

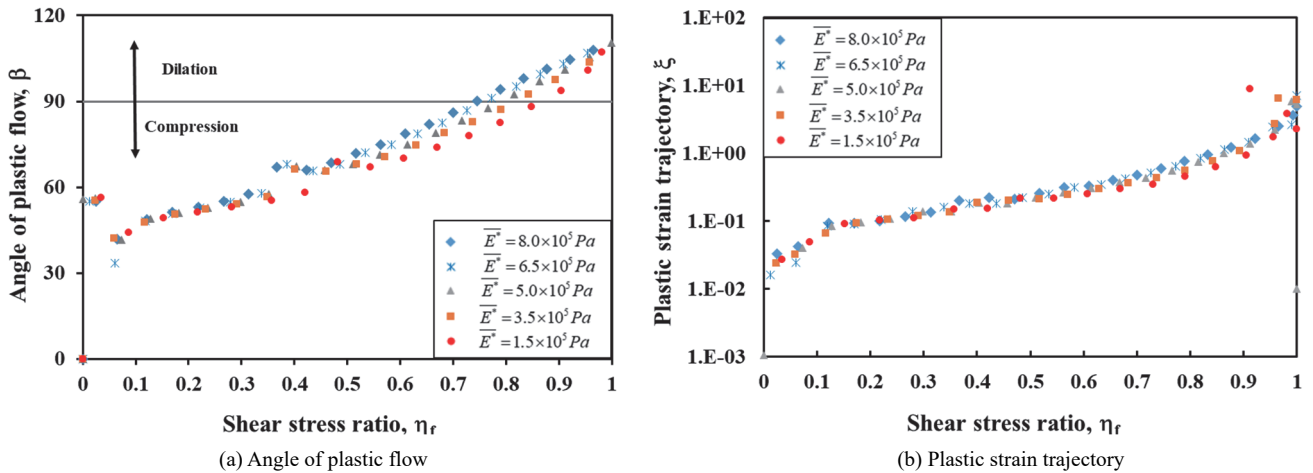

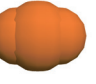



Fig. 18 Effect of bond effective modulus on plastic strain behavior

This study investigated three different particle shapes, which were created in PFC3D using clumps with the same volume. The specific dimensions and aspect ratios are presented in Table 3.

The effect of the aspect ratio on the angle of plastic flow can be observed in Fig. 19(a); the larger the aspect ratio, the larger the plastic flow angle. However, the influence of the AR on the plastic strain trajectory in this study was insignificant (Fig. 19(b)). Furthermore, Table 4 summarizes the influence level of each micro-parameter on the plastic deformation. The micro-parameters, including gravel aspect ratio, porosity, and particle effective modulus, have higher influence on the plastic behavior.

Table 3 The aspect ratio of particles for various shapes

Type of shape		AR	<i>L</i> (mm)	<i>S</i> (mm)
Shape 1		1.0	4.8	4.8
Shape 2		1.2	5.4	4.4
Shape 3		2.0	6.6	3.2

Notes: AR: aspect ratio; *L* and *S*: the longest and shortest particle lengths

Table 4 Summary of effect micro-parameters on the elastoplastic deformation of gravelly soils

Parameters/ Influence level	High	Medium	Low
Plastic flow angle (β)			
Porosity (<i>n</i>)			✓
Friction coefficient (μ)		✓	
Particle effective modulus (E^*)			✓
Bond effective modulus (\bar{E}^*)		✓	
Gravel aspect ratio (AR)	✓		
Plastic strain trajectory (ξ)			
Porosity (<i>n</i>)	✓		
Friction coefficient (μ)		✓	
Particle effective modulus (E^*)	✓		
Bond effective modulus (\bar{E}^*)			✓
Gravel aspect ratio (AR)			✓

5. CONCLUSIONS

Based on the advantages of DEM in granular materials research, this study adopted PFC3D to simulate a large-scale triaxial test to elucidate the deformational behaviors, including nonlinear elastic and significant plastic deformation of gravelly soil. Two types of soil specimens were classified based on matrix properties: with cohesion (group B) and without cohesion (group A). The results revealed that the simulated failure envelopes and stress-strain curves agreed with the test results. For high confining pressures, the results of the experiment and simulation were even more reasonable. The results also exhibit the non-cohesive property of Group A ($c \approx 0$) and the cohesion property of Group B ($c \approx 0.08$ MPa), which agrees with the results of Ho and Weng (2021). In addition, to evaluate the influence of particle shape on the simulation results, this study considers the change in the aspect ratio (AR) of gravel particles while the volume of the particles remains constant. The peak shear strength is enhanced when AR is increased.

The elastoplastic deformation behavior of gravelly soils through the elastic shear modulus and plastic flow was validated with the experimental results. Evidently, the elastic shear modulus of group A is higher than that of group B, and there is a relationship between the shear modulus and confining pressure. Considering the influence of the micro-properties on the elasto-plastic deformation characteristics, the aspect ratio (AR) is the main factor affecting the plastic flow angle. For the plastic strain trajectory analysis, the bond characteristics and AR did not affect the plastic strain trajectory; the porosity and particle effective modulus significantly affected the plastic trajectory; the denser the specimen and the larger E^* , the smaller the plastic strain trajectory.

Notably, this study did not consider the effects of the pore water. The simulated specimens were assumed to be compacted and fully saturated with the initial porosity. The particle in this study was spherical without breakage; the impact of particle shape only focused on the AR of the particles. With the results obtained in the deformation simulation of gravelly soil, the elastoplastic deformation of various gravelly soils can be predicted. Moreover, the microscopic parameters in this study can be used as a reference for foundation simulations of gravelly soils.

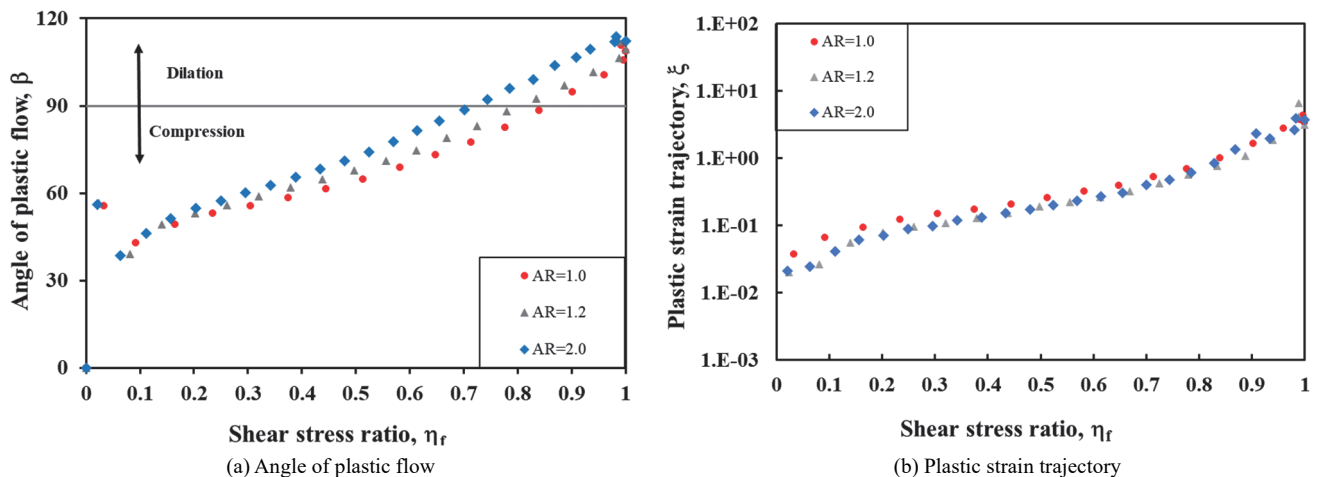


Fig. 19 Effect of aspect ratio on plastic strain behavior

FUNDING

This research was financially supported by the Ministry of Science and Technology, Taiwan under Contract MOST 106-2625-M-390-001, MOST 107-2625-M-009-010, and MOST 108-2628-E-009-004-MY3.

DATA AVAILABILITY STATEMENT

Some or all data, models, or codes that support the findings of this study are available from the corresponding author upon reasonable request.

CONFLICT OF INTEREST STATEMENT

The authors declare that there is no conflict of interest.

REFERENCES

- Bian, X.C., Huang, H., Tutumluer, E., and Gao, Y. (2016). "Critical particle size and ballast gradation studied by discrete element modeling." *Transportation Geotechnics*, **6**, 38-44. <https://doi.org/10.1016/j.trgeo.2016.01.002>
- Bono, J.P.de., McDowell, and G.R. (2014). "DEM of triaxial tests on crushable sand." *Granular Matter*, **16**, 551-562. <https://doi.org/10.1007/s10035-014-0500-x>
- Chang, K.T. and Cheng, M.C. (2014). "Estimation of the shear strength of gravel deposits based on field investigated geological factors." *Engineering Geology*, **171**, 70-80. <https://doi.org/10.1016/j.enggeo.2013.12.014>
- Chang, K.T., Kang, Y.M, Louis, Ge. and Cheng, M.C. (2015). "Mechanical properties of gravelly deposits evaluated by nonconventional methods." *Journal of Materials in Civil Engineering*, ASCE, **27**(11), 04015032. [https://doi.org/10.1061/\(ASCE\)MT.1943-5533.0001287](https://doi.org/10.1061/(ASCE)MT.1943-5533.0001287)
- Cheng, Y.P., Bolton, M.D. and Nakata, Y. (2004). "Crushing and plastic deformation of soils simulated using DEM." *Géotechnique*, **54**(2), 131-141. <https://doi.org/10.1680/geot.2004.54.2.131>
- Chu, B.L., Jou, Y.W. and Weng, M.C. (2010). "A constitutive model for gravelly soils considering shear-induced volumetric deformation." *Canadian Geotechnical Journal*, **47**, 662-673. <https://doi.org/10.1139/T09-135>
- Cil, M.B., Sohn, C., and Buscarnera, G. (2020). "DEM modeling of grain size effect in brittle granular soils." *International Journal of Geomechanics*, ASCE, **146**(3), 04019138. [https://doi.org/10.1061/\(ASCE\)EM.1943-7889.0001713](https://doi.org/10.1061/(ASCE)EM.1943-7889.0001713)
- Coetzee, C.J. and Els, D.N.J. (2009). "Calibration of granular material parameters for DEM modelling and numerical verification by blade-granular material interaction." *Journal of Terramechanics*, **46**, 15-26. <https://doi.org/10.1016/j.jterra.2008.12.004>
- Dahal, B. and Mishra, D. (2020). "Discrete element modeling of permanent deformation accumulation in railroad ballast considering particle breakage." *Frontiers in Built Environment*, **5**(145), 1-14. <https://doi.org/10.3389/fbuil.2019.00145>
- Fattah, M.Y., Abbas, S.F., and Karim, H.H. (2012). "A model for coupled dynamic elasto-plastic analysis of soils." *Journal of GeoEngineering*, **7**(3), 089-096. [http://dx.doi.org/10.6310/jog.2012.7\(3\).2](http://dx.doi.org/10.6310/jog.2012.7(3).2)
- Feng, C.F., Gong, J., Nie, Z.H., Li, B., and Li, X. (2021). "DEM study on the microscale and macroscale shear behaviours of granular materials with breakable and irregularly shaped particles." *Computers and Geotechnics*, **137**, 104271-1 – 104271-13. <https://doi.org/10.1016/j.compgeo.2021.104271>
- Gan, B.R., Yang, X.G., Chen, M.L., and Zhou, J.W. (2018). "Effects of fine particle content and sample scale on the failure properties of loose landslide deposits." *Arabian Journal of Geosciences*, **11**, 152-1-152-11. <https://doi.org/10.1007/s12517-018-3481-y>
- Gan, J.Q. and Yu, A.B. (2020). "DEM simulation of the packing of cylindrical particles." *Granular Matter*, **22**, 22(2020). <https://doi.org/10.1007/s10035-019-0993-4>
- Gong, J. and Liu, J. (2017). "Effect of aspect ratio on triaxial compression of multi-sphere ellipsoid assemblies simulated using a discrete element method." *Particoulogy*, **32**, 49-62. <https://doi.org/10.1016/j.partic.2016.07.007>
- Gong, J., Wang, X., Li, L., and Nie, Z.H. (2019). "DEM study of the effect of fines content on the small-strain stiffness of gap graded soils." *Computers and Geotechnics*, **112**, 35-40. <https://doi.org/10.1016/j.compgeo.2019.04.008>
- Gutiérrez, J.G., Senent, S., Zeng, P., and Jimenez, R. (2021).

- “DEM simulation of rock creep in tunnels using Rate Process Theory.” *Computers and Geotechnics*, **142**, 104559. <https://doi.org/10.1016/j.compgeo.2021.104559>
- Hazzar, L., Nuth, M., and Cherkired, M. (2020). “DEM simulation of drained triaxial tests for glass-beads.” *Journal of Powder Technology*, **364**, 123-134. <https://doi.org/10.1016/j.powtec.2019.09.095>
- Ho, T.K.T. and Weng, M.C. (2021). “Evaluating influence of microscopic properties on mechanical behavior of gravelly soils by using discrete-element method.” *International Journal of Geomechanics*, ASCE, **21**(12), 04021228. [https://doi.org/10.1061/\(ASCE\)GM.1943-5622.0002178](https://doi.org/10.1061/(ASCE)GM.1943-5622.0002178)
- Holtz, W.G. (1961). “Triaxial shear characteristics of clayed gravel soil.” *Proceedings of the 5th International Conferences on Soil Mechanics and Foundation Engineering*, Dunod, Paris, 143-149.
- Hossain, Z., Indrarana, Darve, F., and Thakur, P.K. (2007). “DEM analysis of angular ballast breakage under cyclic loading.” *Geomechanics and Geoengineering*, **2**(3), 175-181. <https://doi.org/10.1080/17486020701474962>
- Indraratna, B., Ionescu, D., and Christie, H.D. (1998). “Shear behavior of railway ballast based on large-scale triaxial tests.” *Journal of Geotechnical and Geoenvironmental Engineering*, ASCE, **124**(5), 439-448. [https://doi.org/10.1061/\(ASCE\)1090-0241\(1998\)124:5\(439\)](https://doi.org/10.1061/(ASCE)1090-0241(1998)124:5(439))
- Itasca Consulting Group Inc. (2016). *PFC—Particle Flow Code*, Version 5.0. Minneapolis: Itasca. <https://www.itascacg.com/software/downloads/pfc-5-00-update>
- Kozicki, J., Tejchman, J., and Mühlhaus, H.B. (2014). “Discrete simulations of a triaxial compression test for sand by DEM.” *International Journal for Numerical and Analytical Methods in Geomechanics*, **38**, 1923-1952. <https://doi.org/10.1002/nag.2285>
- Lan, X., Hou, T.S., Yang, Y., Zhang, Y.F., and Jiang, X.D. (2021). “Numerical simulation on dynamic deformation characteristics of light weight soil with different EPS particle sizes by discrete element method.” *Journal of GeoEngineering*, **16**(3), 111-120. [http://dx.doi.org/10.6310/jog.202109_16\(3\).4](http://dx.doi.org/10.6310/jog.202109_16(3).4)
- Li, Y.L., Wu, W.P., Chu, X.H., and Zou, W.L. (2020). “Effects of stress paths on triaxial compression mechanical properties of QH-E lunar soil simulant studied by DEM simulation.” *Granular Matter*, **22**(2), 1-10. <https://doi.org/10.1007/s10035-020-0999-y>
- Liu, X.Y., Zou, D.G., Liu, J.M., Zheng, B.W., Zhou, C.G., and Bai, J.S. (2021) “A gradation-dependent particle shape factor for characterizing small-strain shear modulus of sand-gravel mixtures.” *Transportation Geotechnics*, **28**, 100548. <https://doi.org/10.1016/j.trgeo.2021.100548>
- Liu, Y. and Jeng, D.S. (2019). “Pore structure of grain-size fractal granular material.” *Materials*, **12**(13), 1-26. <https://doi.org/10.3390/ma12132053>
- Marsal, R.J. (1967). “Strength and deformation characteristics of rockfill materials.” *Journal of the Soil Mechanics and Foundations Division*, **93**, 27-43. https://www.issmge.org/uploads/publications/1/32/1994_03_0007.pdf
- Matheson, G.M. (1986). “Relationship between compacted rock-fill density and gradation.” *Journal of Geotechnical Engineering*, **112**(12), 1119-1124. [https://doi.org/10.1061/\(ASCE\)0733-9410\(1986\)112:12\(1119\)](https://doi.org/10.1061/(ASCE)0733-9410(1986)112:12(1119))
- Minh, N.H. and Cheng, Y.P. (2013). “A DEM investigation of the effect of particle-size distribution on one-dimensional compression.” *Géotechnique*, **63**(1), 44-53. <http://dx.doi.org/10.1680/geot.10.P.058>
- Ngo, T. and Indraratna, B. (2020). “Analysis of deformation and degradation of fouled ballast: experimental testing and DEM modeling.” *International Journal of Geomechanics*, **20**(9), 06020020. <https://orcid.org/0000-0002-9676-3728>
- Nie, Y.X., Gong, J., Fang, C.F., Chen, Z.B., and Huang, C.H. (2023). “DEM study on the macro- and micromechanical behaviours of breakable granular materials under cyclic loading.” *Transportation Geotechnics*, **38**, 100915. <https://doi.org/10.1016/j.trgeo.2022.100915>
- Nitka, M. and Tejchman, J. (2015). “Modelling of concrete behaviour in uniaxial compression and tension with DEM.” *Granular Matter*, **17**, 145-164. <https://doi.org/10.1007/s10035-015-0546-4>
- Potyondy, D.O. and Cundall, P.A. (2004). “A bonded-particle model for rock.” *Journal of Rock Mechanics & Mining Sciences*, **41**, 1329-1364. <https://doi.org/10.1016/j.ijrmms.2004.09.011>
- Qian, J.G., Gu, J.B., Gu, X.Q., Huang, M.S., and Mu, L.L. (2016). “DEM analysis of railtrack ballast degradation under monotonic and cyclic loading.” *Procedia Engineering*, **143**, 1285-1292. <https://doi.org/10.1016/j.proeng.2016.06.137>
- Qu, T.M., Feng, Y.T., Wang, Y., and Wang, M. (2019). “Discrete element modelling of flexible membrane boundaries for triaxial tests.” *Computers and Geotechnics*, **115**, 103154. <https://doi.org/10.1016/j.compgeo.2019.103154>
- Rücknagel, J., Götze, P., Hofmann, B., Christen, O., and Marschall, K. (2013). “The influence of soil gravel content on compaction behaviour and pre-compression stress.” *Geoderma*, **209-210**, 226-232. <https://doi.org/10.1016/j.geoderma.2013.05.030>
- Tian, J.Q., Liu, E.L., Jiang, L., Jiang, X.Q., Sun, Y., and Xu, R. (2018). “Influence of particle shape on the microstructure evolution and the mechanical properties of granular materials.” *Comptes Rendus Mecanique*, **346**, 460-476. <https://doi.org/10.1016/j.crme.2018.03.006>
- Wang, J.W., Chi, S.C., Shao, X.Q., and Zhou, X.X. (2021). “Determination of the mechanical parameters of the microstructure of rockfill materials in triaxial compression DEM simulation.” *Computers and Geotechnics*, **137**, 104625. <https://doi.org/10.1016/j.compgeo.2021.104265>
- Weng, M.C., Chu, B.L., and Ho, Y.L. (2013). “Elastoplastic deformation characteristics of gravelly soils.” *Journal of Geotechnical and Geoenvironmental Engineering*, ASCE, **139**, 947-955. [https://doi.org/10.1061/\(ASCE\)GT.1943-5606.0000827](https://doi.org/10.1061/(ASCE)GT.1943-5606.0000827)
- Weng, M.C. and Li, H.H. (2012). “Relationship between the deformation characteristics and microscopic properties of sandstone explored by the bonded-particle model.” *International Journal of Rock Mechanics and Mining Sciences*, **56**, 34-43. <https://doi.org/10.1016/j.ijrmms.2012.07.003>
- Wu, M.M., Xiong, L.H., and Wang, J.F. (2021). “DEM study on effect of particle roundness on biaxial shearing of sand.” *Underground Space*, **6**, 678-694. <https://doi.org/10.1016/j.undsp.2021.03.006>
- Yang, J. and Wei, L.M. (2012). “Collapse of loose sand with the addition of fines: the role of particle shape.” *Géotechnique*, **62**(12), 1111-1125. <https://doi.org/10.1680/geot.11.P.062>
- Yang, P., Kavazanjian, E., and Neithalath, N. (2019). “Particle-

scale mechanisms in undrained triaxial compression of bio-cemented sands: Insights from 3D DEM simulations with flexible boundary.” *International Journal of Geomechanics*, ASCE, **19**(4), 04019009.
[https://doi.org/10.1061/\(ASCE\)GM.1943-5622.0001346](https://doi.org/10.1061/(ASCE)GM.1943-5622.0001346)

Zhang, F.G., Wang, C.J., Chang, J.M., and Feng, H.P. (2021). “DEM analysis of cyclic liquefaction behaviour of cemented sand.” *Computers and Geotechnics*, **142**, 104572.
<https://doi.org/10.1016/j.compgeo.2021.104572>

